

# Measuring SHmax with Stress-Induced Anisotropy in Nonlinear Anelastic Behavior

Andrew Delorey (✉ [andrew.delorey@lanl.gov](mailto:andrew.delorey@lanl.gov))

Los Alamos National Laboratory <https://orcid.org/0000-0002-5573-8251>

Götz Bokelmann

University of Vienna

Christopher Johnson

Los Alamos National Laboratory

Paul Johnson

Los Alamos National Laboratory

---

## Article

**Keywords:** geophysics, SHmax

**Posted Date:** March 9th, 2021

**DOI:** <https://doi.org/10.21203/rs.3.rs-288404/v1>

**License:** © ⓘ This work is licensed under a Creative Commons Attribution 4.0 International License.

[Read Full License](#)

---

**Version of Record:** A version of this preprint was published at Communications Earth & Environment on September 9th, 2021. See the published version at <https://doi.org/10.1038/s43247-021-00244-1>.

1 **Measuring  $S_{Hmax}$  with Stress-Induced Anisotropy in Nonlinear Anelastic Behavior**

2 **Andrew A. Delorey<sup>1</sup>, Götz H.R. Bokelmann<sup>2</sup>, Christopher W. Johnson<sup>1</sup>,**  
3 **and Paul A. Johnson<sup>1</sup>**

4 **<sup>1</sup>Los Alamos National Laboratory, Mailstop D446, Los Alamos, NM 87545**

5 **<sup>2</sup>Department of Meteorology and Geophysics, University of Vienna**

6

7 **Abstract**

8           Mechanical stress acting in the Earth's crust is a fundamental property that has a wide  
9 range of geophysical applications, from tectonic movements to energy production. The  
10 orientation of maximum horizontal compressive stress,  $S_{Hmax}$  can be estimated by inverting  
11 earthquake source mechanisms and directly from borehole-based measurements, but large  
12 regions of the continents have few or no observations. Available observations often represent a  
13 variety of length scales and depths, and can be difficult to reconcile. Here we present a new  
14 approach to determine  $S_{Hmax}$  by measuring stress induced anisotropy of nonlinear susceptibility.  
15 We observe that nonlinear susceptibility is azimuthally dependent in the Earth and maximum  
16 when parallel to  $S_{Hmax}$ , as predicted by laboratory experiments. Our measurements use empirical  
17 Green's functions that are applicable for different temporal and spatial scales. The method can  
18 quantify the orientation of  $S_{Hmax}$  in regions where no measurements exist today.  
19

## 20 Introduction

21 Knowledge of the mechanical stress acting in the Earth's crust and lithosphere is important  
22 for a wide range of geophysical studies and applications<sup>1-4</sup> including plate tectonics<sup>5,6</sup>, seismicity<sup>7-</sup>  
23 <sup>11</sup> and subsurface fluid behavior<sup>9,12,13</sup>. It is commonly represented as the orientation of the  
24 maximum horizontal compressive stress ( $S_{Hmax}$ )<sup>3,8,14-16</sup>. Other information regarding the principle  
25 components is often not known, much less the full stress tensor. At regional to tectonic-plate  
26 scales, the orientation of  $S_{Hmax}$  is determined by plate boundary forces and tractions along the  
27 bottom of the lithosphere<sup>17</sup>. At local scales (<10 km), the orientation of  $S_{Hmax}$  may vary due to  
28 heterogeneities in density and elasticity, slip on faults<sup>7,12</sup>, and pore pressure<sup>12</sup>. The orientation of  
29  $S_{Hmax}$  is commonly estimated using borehole-based methods<sup>18,19</sup> and inverting earthquake focal  
30 mechanisms<sup>20-24</sup>, and less commonly by measuring the orientation of stress sensitive geologic  
31 features<sup>25</sup>. Borehole-based methods are high-cost, point measurements with unknown  
32 applicability away from the borehole<sup>26</sup>, and commonly applied in hydrocarbon producing regions<sup>8</sup>.  
33 Interpreting earthquake focal mechanisms is limited to seismically-active areas and requires an  
34 adequate monitoring network. Because of the limitations of these techniques, broad regions of  
35 continental interiors are poorly constrained where there are few or no measurements<sup>15</sup>.

36 Rock samples in laboratory experiments typically exhibit anisotropic nonlinear elastic  
37 properties when a uniaxial stress is applied<sup>27,28</sup> (Figure 1). In the laboratory, the pressure derivative  
38 of the wave modulus (called nonlinear susceptibility, NS) is strongest when the angle between the  
39 uniaxial stress and the propagation of the probe wave is zero, and weakest when the angle is 90  
40 degrees. The effect is greatest for compressional P-waves and the nonlinear elastic behavior is  
41 quantified by measuring this behavior. We investigate whether nonlinear elastic properties of the  
42 Earth are sensitive to the orientation of  $S_{Hmax}$  because of anisotropy in rock compressibility.

43           Rocks are heterogeneous materials with stress and strain dependent elastic properties, and  
44 finite, nonzero relaxation times (the slow dynamics)<sup>29-31</sup>. The relationship between stress, strain,  
45 and elasticity is complex in individual rock samples<sup>32,33</sup> with mechanical damage and weak grain  
46 contacts being primarily responsible for nonlinear elastic behavior<sup>34</sup>. Temperature, pressure, and  
47 the presence of fluids modulate the nonlinear behavior<sup>34,35</sup>. In the Earth, seismic velocities are  
48 commonly observed to be faster when rocks are compressed, usually interpreted as the closing of  
49 cracks<sup>36,37</sup>, while they are typically slower after experiencing strong shaking, usually interpreted  
50 as the breaking or weakening of internal contacts<sup>38,39</sup>. After the disturbance, the material relaxes  
51 back to its original or a new metastable state, the process of slow dynamics. Thus, rocks are  
52 metastable in their elastic behavior and strongly influenced by relatively weak external forces  
53 perturbing the material structure<sup>35,38,39</sup>.

54           We utilize this nonlinear elastic behavior in rocks and apply a new technique to passively  
55 monitor the orientation of stress in the lithosphere. Our approach to measure  $S_{Hmax}$  *in situ* relies on  
56 seismic velocity measurements that employ Empirical Green's Functions (EGF) derived from  
57 ambient noise recorded at multiple pairs of seismic stations<sup>40</sup>. Most studies in Earth that measure  
58 temporal changes in seismic velocities do so by differencing the phase in the coda part of the  
59 EGF<sup>36,38,39</sup>. The coda of the EGF follows the direct waves and is the result of scattered waves that  
60 travel through some volume between the two stations<sup>41</sup>. We can measure the velocity sensitivity  
61 to strain using a classic nonlinear acoustic approach known as the pump-probe method<sup>33</sup> where the  
62 material is strained with a low-frequency oscillation (pump) and the elasticity is monitored by  
63 measuring the travel time of a high frequency probe wave that is applied at different points in the  
64 pump cycle.

65           For this study, solid Earth tides are used as the low-frequency pump and EGFs are the high  
66 frequency probe. We perform this natural pump-probe experiment in two prototype studies located

67 in north-central Oklahoma, U.S.A. and north-central New Mexico, U.S.A. (Figure 2). We selected  
68 north-central Oklahoma because of the ongoing induced seismicity, generated by decades of  
69 injected wastewater from oil and gas operations<sup>42,43</sup>, that tends to occur on faults optimally  
70 orientated in the regional stress field<sup>9</sup>. North-central New Mexico was selected to test if we can  
71 resolve similar results in a geologic setting that straddles a continental rift and has a different stress  
72 field than Oklahoma<sup>16,44</sup> (Figure 2). In north-central Oklahoma,  $S_{Hmax}$  is oriented approximately  
73 N80E with some local variations<sup>9</sup>, but in north-central New Mexico,  $S_{Hmax}$  is aligned nearly south-  
74 north along the Rio Grande Rift and rotates to a more east-west orientation in northeastern New  
75 Mexico<sup>16</sup>. The dominant faulting style in Oklahoma is strike-slip, though there is some normal  
76 faulting in the north in the vicinity of our study area while the faulting style is strongly normal  
77 faulting in northern New Mexico, associated with the Rio Grande Rift<sup>8</sup>.

78         The Earth exhibits stress induced anisotropy of nonlinear susceptibility (NS) that is aligned  
79 with  $S_{Hmax}$  in two different geologic settings, matching observations from the laboratory when a  
80 uniaxial stress is applied to laboratory rock samples. Since our measurements use only ambient  
81 seismic noise, there are several advantages over existing methods for estimating the orientation of  
82  $S_{Hmax}$ : (1) earthquake source properties are not used or required, (2) borehole measurements are  
83 not required, (3) sufficient seismic data exists in many regions of interest where traditional stress  
84 measurements are unavailable, and (4) the technique can be applied at a wide range of spatial and  
85 temporal scales.

## 86 **Results**

87         In both study areas, on average, the Earth is slower during extension than during  
88 compression by fractional velocities of 0.07% and 0.2% with uncertainties of 10% of the velocity  
89 change, for Oklahoma and New Mexico, respectively. This is consistent with the opening and  
90 closing of cracks, and the stiffening of internal contacts during compression. In Figure 3, we

91 report NS as fractional velocity change, though NS is actually fractional velocity change per unit  
92 strain. Tidal strain is on the order  $10^{-8}$  and it varies somewhat from cycle-to-cycle. Our results  
93 reflect the average peak-to-peak strain amplitude, which is discussed below.

#### 94 **Oklahoma**

95 In Oklahoma, a fitted sine function to the results shows the maximum (negative  
96 magnitude) nonlinear NS occurs between  $69^{\circ}$ - $86^{\circ}$ , depending upon the selection of stations.  
97 Borehole measurements and a focal mechanism inversion estimate  $S_{Hmax}$  orientations between  
98  $71^{\circ}$ - $84^{\circ}$  in the same region<sup>9</sup>. In this previous study, the reported  $S_{Hmax}$  azimuth is lower in the  
99 north than in the south (rotated counter-clockwise), and consistent with the values we observe  
100 from the maximum NS, see Figure 1 and Table 1 in Alt and Zoback (2017)<sup>9</sup>. Comparing our  
101 results to stress indicators used in the World Stress Map<sup>25</sup> (shown in Figure 2), our results are  
102 more consistent with borehole than earthquake measurements, which are inconstant with each  
103 other in some places. We note that considering only some of the northern stations produces  
104 ambiguous results. This ambiguity and a few positive values in Figure 3, indicating that  
105 velocities are faster during extension, may be the result of poroelastic effects and are discussed in  
106 more detail below.

#### 107 **New Mexico**

108 In New Mexico, a fitted sine function to the results using all stations shows the maximum  
109 (negative magnitude) NS occurs at  $178^{\circ}$  (Figure 4). The maximum NS using only the 6  
110 westernmost stations is  $8^{\circ}$  and using only the 6 easternmost stations is  $163^{\circ}$ , with the 3 central  
111 stations used in both subarrays. The regional stress indicators show a transition, moving west to  
112 east, from slightly southwest-northeast to south-north  $S_{Hmax}$  orientation within the Rio Grande  
113 Rift (Figure 2). Continuing east, a southeast-northwest  $S_{Hmax}$  orientation is expected, although no  
114 known stress indicators are available within this transition zone. Considering the 6 western

115 stations, the NS predicts  $S_{Hmax}$  at  $8^\circ$ , which is consistent with stress indicators within the rift  
116 valley and mountains to the west. Using the 6 easternmost stations, NS predicts  $S_{Hmax}$  at  $163^\circ$ ,  
117 which is rotated counterclockwise from the results of the western stations, and intermediate  
118 between the reported stress indicators within the Rio Grande Rift and the reported southeast-  
119 northwest stress indicators east of the study area. Our NS derived  $S_{Hmax}$  results for all 9 stations  
120 are in agreement with the average orientation of stress indicators within the footprint of the  
121 seismic array. Since no stress indicators exist for the eastern part of the study area, our results  
122 using the eastern stations suggest the observed clockwise rotation from east to west transitions  
123 into our study area. The results provide a clear example of constraining the stress field using  
124 passive seismic data in a region where no other estimates are available.

## 125 **Discussion**

126 The azimuthal dependence of NS closely tracks the orientation of  $S_{Hmax}$  in the Earth as  
127 shown in the laboratory<sup>27,28</sup>. In terms of elastic constants, what we measure is closely related to  
128 the 1-D nonlinear anelastic coefficient  $\beta$  which is the coefficient linearly related to strain in a  
129 Taylor expansion of Hooke's law (see, e.g., equations 7 and 8 in Johnson and Rasolofosaon<sup>27</sup>  
130 and Pantea et al.<sup>45</sup>). In single crystals and metals  $\beta$  is less than 10. In Earth materials it can be  
131 considerably larger, order  $10^2$ - $10^3$  underscoring how very nonlinear elastic Earth materials can  
132 be. In the laboratory experiments, stress induced anisotropy is strongest for P-waves<sup>28</sup>, which  
133 suggests our measurements describe the scattered compressional-wave energy either in the form  
134 of Rayleigh waves or P-body waves. Since our measurements are made with the vertical  
135 channels of a seismic station pair, we are measuring a specific component of the nonlinear  
136 coefficient  $\beta$ , which may be better represented as a tensor. Exploring the possible tensor  
137 properties of  $\beta$  is beyond the scope of this study but may be possible by developing a 6

138 component NS tensor using all combination of station channels. Such a measurement would be  
139 very useful in discerning the anisotropic mechanical damage variations in the upper crust.

140 The difference in strain between maximum extension and maximum compression for  
141 solid Earth tides is of the order  $5 \times 10^{-8}$ , which means the observed NS ( $dv/d\epsilon$ , change in velocity  
142 over change in strain) is of the order  $10^4$ - $10^5$ . These results are similar in magnitude to those  
143 found by Takano et al.<sup>46</sup> near a volcano in Japan using EGF frequencies of 1-2 Hz, and an order  
144 of magnitude higher than those found by Hillers et al.<sup>47</sup> in California using frequencies of 2-8  
145 Hz. In these two previous studies, the authors measured nonlinearity, but did not report  
146 azimuthal differences, nor the relationship between nonlinearity and stress-induced anisotropy.

147 In addition to the opening and closing of cracks in dry conditions, resulting in the  
148 softening and stiffening of internal contacts, there may be poroelastic effects. Under saturated  
149 conditions, pore pressure increases during applied compression and decreases during applied  
150 extension, with pore pressure having the opposite effect on the effective confining stress as the  
151 applied tidal stress. This effect is expected to be isotropic in most rocks<sup>48</sup>. If all station pairs in  
152 an array experience the same poroelastic conditions, the effect of stress-induced anisotropy is  
153 preserved, though curves shown in Figure 3 would shift upward (positive). In some cases we  
154 could even see positive values<sup>47</sup>. If different station pairs experience different poroelastic  
155 effects, this would complicate the estimation of  $S_{Hmax}$  since the observed azimuthal dependence  
156 of NS would no longer be due only to stress-induced anisotropy. In Oklahoma, we are able to  
157 get good estimates for  $S_{Hmax}$  despite likely contributions from heterogeneous poroelastic  
158 conditions<sup>49</sup> that are apparent when using a fewer number of station pairs. This may be why  
159 using only northern stations in Oklahoma produces ambiguous results, and that the sinusoidal fit  
160 is generally worse when using a fewer number of station pairs in Figures 3 and 4.

161 Measuring and modeling stress in the Earth's crust is challenging and it is important to  
162 match the length scale and depth to the desired application. Since stress heterogeneity likely  
163 exists at all scales<sup>10,20,26</sup>, a measured stress or  $S_{Hmax}$  may not be representative of different length  
164 scales or depths. Our method has the potential to address some of these challenges. EGFs can  
165 be calculated using varying interstation distances to provide  $S_{Hmax}$  estimates at different  
166 horizontal length scales. Estimating  $S_{Hmax}$  at specific depths is more challenging but possible  
167 when using relative depths inferred through frequency content and coda time offset in the  
168 EGFs<sup>38,41</sup> but is a promising area of research. Perhaps most importantly, measuring the  
169 orientation of  $S_{Hmax}$  is not limited to locations with earthquakes or boreholes, and provides data  
170 driven constraints to regional estimates. Additional possibilities include calculating the time  
171 evolution of NS to obtain  $S_{Hmax}$ , which could reveal changes in relative amplitude and  
172 orientation. Temporal monitoring of subsurface fluid reservoirs or active fault zones may  
173 represent changes in pore pressures or fault zone properties during the loading cycle.

174 Long wavelength stress and deformation patterns in tectonic plates are generated from  
175 global scale mantle convection<sup>50</sup>. Smaller-scale patterns are related to the gravitational potential  
176 of a heterogeneous crust and lithosphere<sup>51</sup>, or small-scale convection in the mantle<sup>52</sup>. The  
177 relative contribution of these two mechanisms is unknown. Ultimately, we do not know to what  
178 extent continental-scale stress models represent the actual stress field in regions with few or no  
179 measurements to constrain these estimates. Therefore, we cannot attempt to model or  
180 characterize mechanisms for these unknown heterogeneities. This method provides a dense and  
181 uniform metric of the orientation of  $S_{Hmax}$  across continental regions, which will improve stress  
182 models and our understanding of the underlying geodynamical processes.

183 We calculated EGFs as a function of tidal strain and azimuth in north-central Oklahoma  
184 and north-central New Mexico to constrain NS and derive the orientation of  $S_{Hmax}$ . Our results

185 show in both study areas the seismic velocities are, on average, faster when the Earth is in  
186 compression relative to when the Earth is in extension. We observe stress induced anisotropy in  
187 nonlinear anelastic behavior, which is aligned with  $S_{Hmax}$  and provides a new technique to  
188 estimate the orientation of  $S_{Hmax}$  without focal mechanism inversions or borehole measurements.  
189 Large scale application of this method may resolve additional tensor properties of the nonlinear  
190 coefficient  $\beta$ , reveal how  $S_{Hmax}$  varies with horizontal length scales and depth, and how  $S_{Hmax}$   
191 evolves temporally in regions such as fluid reservoirs and active fault zones.  
192

## 193 **Methods and Data**

194           We use publicly available seismic data from the two study areas, north-central Oklahoma  
195 and north-central New Mexico. For Oklahoma, we obtained waveform data recorded by the  
196 Nanometrics Research Array (NX) from the Incorporated Research Institutions for Seismology  
197 Data Management Center (IRIS-DMC, [www.iris.edu](http://www.iris.edu)). The NX array consists of 30 broadband,  
198 3-component instruments that recorded at 100 samples per second for about three years between  
199 mid-2013 and mid-2016 (red circles in Figure 2). For New Mexico, we obtained waveform data  
200 from 9 stations in Earthscope’s Transportable Array (TA) from the IRIS-DMC. This subarray  
201 consists of 9 broadband, 3-component instruments that recorded at 40 samples per second for about  
202 two years between mid-2008 and mid-2010 (blue circles in Figure 2). We used only the vertical  
203 component for all seismic data.

## 204 **Signal Processing**

205           We organize the data into day-long segments and deconvolve the instrument response.  
206 When calculating EGFs from continuous broadband seismic data it is important to remove  
207 transient signals like earthquakes<sup>53</sup>. We remove earthquake signals from the data using the U.S.  
208 Geological Survey Comprehensive Catalog. We assign zeros with a taper for the waveform  
209 segments following three sets of earthquake criteria: (1) earthquakes with a minimum magnitude  
210 of 3.5 and maximum distance of 30 km from the array, between surface wave velocities of 2 and  
211 5 km/s, (2) earthquakes with a minimum magnitude 5 and maximum distance of 2000 km from  
212 the array, between surface wave velocities of 2 and 7 km/s, and (3) earthquakes with a minimum  
213 magnitude of 6 at any distance, between surface wave velocities of 2 and 8 km/s. This resulted in  
214 the zeroing of 7.9% of waveforms for Oklahoma and 4.3% of waveforms for New Mexico. The  
215 disparity exists because there are more local earthquake in Oklahoma than in New Mexico.

216 Additionally, we clip all signals greater than 3 times RMS for each day-long segment to remove  
217 non-earthquake signals observed as emergent or impulsive noise.

## 218 **Tidal Strain**

219 The volumetric tidal strain is obtained using the software package SPOTL<sup>54</sup>. We use the  
220 volumetric strain component because we expect the nonlinear behavior to be localized on pre-  
221 existing faults, which may be at any orientation. We divided time into segments that fit in two  
222 strain magnitude bins, the top 25% and the bottom 25% where “top” refers to maximum extension  
223 and “bottom” refers to maximum compression.

## 224 **Empirical Green’s Functions**

225 We cut and merge the day long preprocessed waveforms into segments appropriate for  
226 each stress bin and discard anything shorter than 30 minutes. We empirically determined that a  
227 station separation distance between 30 and 60 km produce the best EGFs for Oklahoma and  
228 selected station pairs accordingly. For the New Mexico stations we used all pairs. We  
229 calculated an EGF for each selected station pair, and segment for all bins using a phase cross  
230 correlation method<sup>55</sup> where we pre-whiten the spectrum before applying a phase cross  
231 correlation. There are approximately 780 segments for each station pair during the recording  
232 period, though the actual number for each pair varies based on data availability, data quality, and  
233 other factors.

234 Next, we describe the EGF stacking procedure (Figure 5). For each station pair we selected  
235 14 day windows, and using the center of the window, selected all EGFs whose segment start time  
236 falls within +/- 7 days. Each EGF is scaled by the square root of the duration of the underlying  
237 time series and are all stacked. We calculate the Pearson correlation coefficient of each EGF with  
238 the stack. Any EGF that has a value of less than 0.5 is discarded and we produce a new stack with  
239 the remaining EGFs. We reevaluate the discarded EGFs and any that have a Pearson correlation

240 coefficient greater 0.5 using the updated stack is re-included to create a new stack. The process is  
241 repeated until there are no discarded EGFs with a Pearson correlation coefficient greater than 0.5.  
242 Subsequent 14 day windows are calculated with a 7 day overlap. This stacking procedure is  
243 intended to include as many observations as possible while discarding outliers. The outcome is  
244 stacked EGFs for each station pair that represent 14 day windows with 7 day overlap for each of  
245 the two strain bins described above.

246 We sum the causal and acausal parts of the EGF and select the coda part as shown in Figure  
247 5 to avoid direct wave arrivals. We determine the average phase difference and velocity change  
248 ( $\Delta v/v$ ) between two stacked EGFs in a 30 second coda window for waves between 4 and 5 seconds  
249 period following the steps outlined in the wavelet method of Mao et al.<sup>56</sup>. We used a Morlet  
250 wavelet with  $\omega_0 = 0.25$  Hz that corresponds to the periods we analyzed and allows us to recover  
251 the known phase shifts in simple synthetic examples. This method has the ability to measure phase  
252 shifts associated with changes in velocity as a function of frequency and coda offset time, but we  
253 are only interested and present the average velocity changes. Results measured by frequency and  
254 coda offset time likely contain depth information<sup>38,41,56</sup> but are beyond the scope of this study.  
255 Along with measuring phase shifts, we also calculate coherence between the two EGF stacks and  
256 discard any cases where the average coherence falls below 0.95. In our convention a negative  
257 ( $\Delta v/v$ ) value means that the Earth is slower during extension than during compression, which we  
258 tested with synthetic examples.

259 The coda part of the EGF consists of scattered waves that are composed of surface waves  
260 and body waves. In general, the earlier part of the coda contains more scattered surface waves,  
261 while the later part contains more body waves, with the transition time governed by the scattering  
262 properties of the subsurface<sup>41</sup>. If the window of the measurements contains mostly surface waves,  
263 they are sensitive to the upper 2-3 km for Rayleigh waves between 4-5 second periods. If the

264 window of the measurements contains mostly body waves, then the waves would be sensitive over  
265 a greater depth range, depending on the velocity of the scattered waves, and the scattering  
266 properties in the subsurface.

267 We group and stack the station pairs by azimuth to examine any directional dependence to  
268 the results. The azimuth for each pair is determined using the relationship between the more  
269 western station to the more eastern station so that values are always between 0 and 180, with 0 and  
270 180 indicating south-north and 90 indicating west-east. For Oklahoma, we consider 9 azimuths in  
271 20 degree steps. For each azimuthal interval, we average the  $dv/v$  values for all pairs whose  
272 azimuth is within  $\pm 20$  degrees with wrapping. For example at an azimuth of 0 degree, we  
273 average paths between 0 and 20 plus between 160 and 180 degrees (which is equivalent to between  
274 -20 and 0 degree). For New Mexico we consider all station pairs individually because there are  
275 not enough station pairs to average in azimuthal bins. In addition to calculating the average  $\Delta v/v$   
276 at different azimuths, we fit a sine function, periodic on  $2\theta$ , to the results.

277 Uncertainties in our measurements are difficult to precisely estimate. When calculating  
278 EGFs, there is an intrinsic assumption that noise sources are equipartitioned, white, azimuthally  
279 uniform, and stationary. This is never true in the Earth, but we can take steps to reduce the  
280 influence of recordings that violate these assumptions. We assume that velocities in our study  
281 area vary measurably by no more than the amounts observed in other studies, less than  $\pm$   
282 1%<sup>39,46,47</sup>. Since we never directly compare data that has been recorded more than 14 days apart,  
283 seasonal variations are not expected to be important, including spectral content, azimuthal  
284 variations, and relative amounts of coherent and incoherent noise. By discarding EGFs that are  
285 not well-correlated and coda that are not highly coherent we avoid noise or signals that are not  
286 stationary. In both study areas, we stack over two years of data. The resulting uncertainty based

287 on the variance in the accepted measurements suggests that uncertainties are at least an order of  
288 magnitude less than the magnitude of the measurements.

289

290 **Data Availability**

291 All data used in this study are available through the Incorporated Institutions for  
292 Seismology Data Management Center ([www.iris.edu](http://www.iris.edu)).

293 **Acknowledgements**

294 AAD and CWJ were supported by Institutional Support at Los Alamos National Laboratory  
295 (LDRD). PAJ was supported by US Department of Energy, Office of Science, Office of Basic  
296 Energy Sciences, Chemical Sciences, Geosciences, and Biosciences Division Grant  
297 89233218CNA000001. AAD would like to thank the Department of Meteorology and  
298 Geophysics at the University of Vienna for hosting him during this study.

299 **Author Contributions**

300 AAD and GHRB conceived the experiment, AAD performed all calculations, and  
301 contributed to the writing of this manuscript. PAJ, GHRB, and CWJ contributed to the  
302 interpretation of the results and the writing of this manuscript.

303 **Competing Interests**

304 The authors have no competing interests.

305 **Figure 1.**

306 Stress induced anisotropy in Nonlinear Susceptibility from Johnson and Rasolofosaon<sup>27</sup>. The  
307 vertical axis represents nonlinear susceptibility. The horizontal axis shows the angle between the  
308 orientation of the uniaxial stress and the direction of propagation of the probe wave. (AGU  
309 grants permission for individuals to use figures, tables, and short quotes from AGU journal and  
310 books for republication in academic works provided full attribution is included.)

311 **Figure 2.**

312 We measured the azimuthal dependence of nonlinear elastic behavior in north-central New  
313 Mexico and north-central Oklahoma. The blue circles are seismic stations from Earthscope's  
314 Transportable Array. The red circles are seismic stations from the Nanometrics Research Array.  
315 The short black lines indicate the direction of  $S_{Hmax}$  for stress indicators used in the 2016 World  
316 Stress Map, classes A, B, and C. The thick stress indicator lines are from borehole  
317 measurements and the thin stress indicator lines are from earthquake or geologic feature  
318 orientations. The rectangle in the top map indicates the position of the bottom map within North  
319 America.

320 **Figure 3.**  
321 Shown are the seismic stations and azimuthal dependence of nonlinear susceptibility in  
322 Oklahoma. Red stations in the left panels are used to calculate fractional velocity changes shown  
323 on the right (see Fig. 2 for station locations). Vertical red bars represent uncertainties at the  
324 99.5% confidence interval. The orange curve is the best fit sinusoidal function. The value listed  
325 is the azimuthal angle of maximum nonlinear susceptibility according to the fit sinusoid  
326 (negative fractional velocity changes).

327 **Figure 4.**

328 Shown is the azimuthal dependence of nonlinear susceptibility in New Mexico. The left, center,  
329 and right axes show the results using the 6 western stations, all stations, and the 6 eastern  
330 stations, respectively. The orange curve is the best fit sinusoidal function. The vertical red bars  
331 represent the fractional velocity change with uncertainties at the 99.5% confidence level for each  
332 station pair. The angle value reported on each axis indicates the azimuth with the maximum NS  
333 (negative fractional velocity change).

334 **Figure 5.**  
335 Empirical Green's Functions, for Oklahoma (left), and New Mexico (right), ordered by inter-  
336 station distance. The black lines bracket the coda used for the velocity calculations.

337 **References**

- 338 1. Heidbach, O., Rajabi, M., Reiter, K., Ziegler, M. & WSM Team. World Stress Map Database  
339 Release 2016. (2016) doi:10.5880/wsm.2016.001.
- 340 2. McGarr, A. & Gay, N. C. State of stress in the Earth's crust. *Annual Review of Earth and*  
341 *Planetary Sciences* **6**, 405–436 (1978).
- 342 3. Zoback, M. & Zoback, M. State of stress in the conterminous United States. *Journal of*  
343 *Geophysical Research: Solid Earth* **85**, 6113–6156 (1980).
- 344 4. Humphreys, E. D. & Coblenz, D. D. North American dynamics and western U.S. tectonics.  
345 *Rev. Geophys.* **45**, RG3001 (2007).
- 346 5. Richardson, R. M., Solomon, S. C. & Sleep, N. H. Tectonic stress in the plates. *Reviews of*  
347 *Geophysics* **17**, 981–1019 (1979).
- 348 6. Rivera, L. & Kanamori, H. Spatial heterogeneity of tectonic stress and friction in the crust.  
349 *Geophysical Research Letters* **29**, 12-1-12-4 (2002).
- 350 7. Wesson, R. L. & Boyd, O. S. Stress before and after the 2002 Denali fault earthquake.  
351 *Geophysical Research Letters* **34**, L07303 (2007).
- 352 8. Lund Snee, J.-E. & Zoback, M. D. State of stress in Texas: Implications for induced seismicity:  
353 STATE OF STRESS IN TEXAS. *Geophys. Res. Lett.* **43**, 10,208-10,214 (2016).
- 354 9. Alt, R. C. & Zoback, M. D. In Situ Stress and Active Faulting in Oklahoma. *Bulletin of the*  
355 *Seismological Society of America* **107**, 216–228 (2017).
- 356 10. Iio, Y. *et al.* Which is heterogeneous, stress or strength? An estimation from high-density  
357 seismic observations. *Earth, Planets and Space* **69**, 144 (2017).
- 358 11. Hardebeck, J. L. & Okada, T. Temporal Stress Changes Caused by Earthquakes: A Review.  
359 *Journal of Geophysical Research: Solid Earth* **123**, 1350–1365 (2018).
- 360 12. Segall, P. Earthquakes triggered by fluid extraction. *Geology* **17**, 942–946 (1989).

- 361 13. Goebel, T. H. W., Weingarten, M., Chen, X., Haffener, J. & Brodsky, E. E. The 2016  
362 Mw5.1 Fairview, Oklahoma earthquakes: Evidence for long-range poroelastic triggering at 40  
363 km from fluid disposal wells. *Earth and Planetary Science Letters* **472**, 50–61 (2017).
- 364 14. Heidbach, O. *et al.* Global crustal stress pattern based on the World Stress Map database  
365 release 2008. *Tectonophysics* **482**, 3–15 (2010).
- 366 15. Heidbach, O., Rajabi, M., Reiter, K., Ziegler, M. & Team, W. World Stress Map 2016.  
367 (2016).
- 368 16. Lund Snee, J.-E. & Zoback, M. D. Multiscale variations of the crustal stress field  
369 throughout North America. *Nat Commun* **11**, 1951 (2020).
- 370 17. Turcotte, D. L., Schubert, G. & Turcotte, D. L. *Geodynamics*. (Cambridge University  
371 Press, 2002).
- 372 18. Ljunggren, C., Chang, Y., Janson, T. & Christiansson, R. An overview of rock stress  
373 measurement methods. *International Journal of Rock Mechanics and Mining Sciences* **40**, 975–  
374 989 (2003).
- 375 19. Lin, H. *et al.* A Review of In Situ Stress Measurement Techniques. *Coal Operators’*  
376 *Conference* (2018).
- 377 20. Hsu, Y.-J., Rivera, L., Wu, Y.-M., Chang, C.-H. & Kanamori, H. Spatial heterogeneity of  
378 tectonic stress and friction in the crust: new evidence from earthquake focal mechanisms in  
379 Taiwan. *Geophys J Int* **182**, 329–342 (2010).
- 380 21. Michael, A. J. Use of focal mechanisms to determine stress: A control study. *J. Geophys.*  
381 *Res.* **92**, 357 (1987).
- 382 22. Vavryčuk, V. Iterative joint inversion for stress and fault orientations from focal  
383 mechanisms. *Geophysical Journal International* **199**, 69–77 (2014).

- 384 23. de Vicente, G. *et al.* Inversion of moment tensor focal mechanisms for active stresses  
385 around the microcontinent Iberia: Tectonic implications: INVERSION OF FOCAL  
386 MECHANISMS IN IBERIA. *Tectonics* **27**, (2008).
- 387 24. Hardebeck, J. L. & Michael, A. J. Damped regional-scale stress inversions: Methodology  
388 and examples for southern California and the Coalinga aftershock sequence: DAMPED  
389 REGIONAL-SCALE STRESS INVERSIONS. *J. Geophys. Res.* **111**, n/a-n/a (2006).
- 390 25. Heidbach, O. *et al.* The World Stress Map database release 2016: Crustal stress pattern  
391 across scales. *Tectonophysics* **744**, 484–498 (2018).
- 392 26. Schoenball, M. & Davatzes, N. C. Quantifying the heterogeneity of the tectonic stress field  
393 using borehole data. *Journal of Geophysical Research: Solid Earth* **122**, 6737–6756 (2017).
- 394 27. Johnson, P. A. & Rasolofosaon, P. N. J. Nonlinear elasticity and stress-induced anisotropy  
395 in rock. *J. Geophys. Res.* **101**, 3113–3124 (1996).
- 396 28. Nur, A. & Simmons, G. Stress-induced velocity anisotropy in rock: An experimental study.  
397 *J. Geophys. Res.* **74**, 6667–6674 (1969).
- 398 29. Guyer, R. A. & Johnson, P. A. Nonlinear Mesoscopic Elasticity: Evidence for a New Class  
399 of Materials. *Physics Today* **52**, 30–36 (1999).
- 400 30. Yamamura, K. *et al.* Long-term observation of in situ seismic velocity and attenuation: IN  
401 SITU SEISMIC VELOCITY AND ATTENUATION MEASUREMENT. *J. Geophys. Res.* **108**,  
402 (2003).
- 403 31. Niu, F., Silver, P. G., Daley, T. M., Cheng, X. & Majer, E. L. Preseismic velocity changes  
404 observed from active source monitoring at the Parkfield SAFOD drill site. *Nature* **454**, 204–  
405 208 (2008).

- 406 32. Rivière, J., Shokouhi, P., Guyer, R. A. & Johnson, P. A. A set of measures for the  
407 systematic classification of the nonlinear elastic behavior of disparate rocks: RIVIÈRE ET AL.  
408 *J. Geophys. Res. Solid Earth* **120**, 1587–1604 (2015).
- 409 33. Renaud, G., Le Bas, P.-Y. & Johnson, P. A. Revealing highly complex elastic nonlinear  
410 (anelastic) behavior of Earth materials applying a new probe: Dynamic acoustoelastic testing:  
411 A NEW PROBE FOR ELASTICITY IN ROCKS. *J. Geophys. Res.* **117**, 17 (2012).
- 412 34. Guyer, R. A. & Johnson, P. A. *Nonlinear Mesoscopic Elasticity The Complex Behaviour*  
413 *of Granular Media including Rocks and Soil.* (2009).
- 414 35. Shokouhi, P. *et al.* Dynamic stressing of naturally fractured rocks: on the relation between  
415 transient changes in permeability and elastic wave velocity. *Geophys. Res. Lett.* 2019GL083557  
416 (2019) doi:10.1029/2019GL083557.
- 417 36. Delorey, A. A., Chao, K., Obara, K. & Johnson, P. A. Cascading elastic perturbation in  
418 Japan due to the 2012  $M_w$  8.6 Indian Ocean earthquake. *Sci. Adv.* **1**, e1500468 (2015).
- 419 37. Rivet, D. *et al.* Seismic velocity changes, strain rate and non-volcanic tremors during the  
420 2009–2010 slow slip event in Guerrero, Mexico. *Geophysical Journal International* **196**, 447–  
421 460 (2014).
- 422 38. Wu, C. *et al.* Constraining depth range of S wave velocity decrease after large earthquakes  
423 near Parkfield, California: DEPTH RANGE OF S WAVE VELOCITY DECREASE. *Geophys.*  
424 *Res. Lett.* **43**, 6129–6136 (2016).
- 425 39. Brenguier, F. *et al.* Postseismic Relaxation Along the San Andreas Fault at Parkfield from  
426 Continuous Seismological Observations. *Science* **321**, 1478–1481 (2008).
- 427 40. Shapiro, N. M. & Campillo, M. Emergence of broadband Rayleigh waves from correlations  
428 of the ambient seismic noise: CORRELATIONS OF THE SEISMIC NOISE. *Geophys. Res.*  
429 *Lett.* **31**, (2004).

- 430 41. Obermann, A., Planès, T., Larose, E., Sens-Schönfelder, C. & Campillo, M. Depth  
431 sensitivity of seismic coda waves to velocity perturbations in an elastic heterogeneous medium.  
432 *Geophysical Journal International* **194**, 372–382 (2013).
- 433 42. Ellsworth, W. L. Injection-Induced Earthquakes. *Science* **341**, 1225942–1225942 (2013).
- 434 43. Keranen, K. M., Weingarten, M., Abers, G. A., Bekins, B. A. & Ge, S. Sharp increase in  
435 central Oklahoma seismicity since 2008 induced by massive wastewater injection. *Science* **345**,  
436 448–451 (2014).
- 437 44. Kelley, V. C. Tectonics, Middle Rio Grande Rift, New Mexico. in *Special Publications*  
438 (ed. Riecker, R. E.) 57–70 (American Geophysical Union, 2013). doi:10.1029/SP014p0057.
- 439 45. Pantea, C., Osterhoudt, C. F. & Sinha, D. N. Determination of acoustical nonlinear  
440 parameter  $\beta$  of water using the finite amplitude method. *Ultrasonics* **53**, 1012–1019 (2013).
- 441 46. Takano, T., Nishimura, T., Nakahara, H., Ohta, Y. & Tanaka, S. Seismic velocity changes  
442 caused by the Earth tide: Ambient noise correlation analyses of small-array data. *Geophys. Res.*  
443 *Lett.* **41**, 6131–6136 (2014).
- 444 47. Hillers, G. *et al.* In situ observations of velocity changes in response to tidal deformation  
445 from analysis of the high-frequency ambient wavefield. *J. Geophys. Res. Solid Earth* **120**, 210–  
446 225 (2015).
- 447 48. Beeler, N. M., Simpson, R. W., Hickman, S. H. & Lockner, D. A. Pore fluid pressure,  
448 apparent friction, and Coulomb failure. *J. Geophys. Res.* **105**, 25533–25542 (2000).
- 449 49. Walsh, F. R. & Zoback, M. D. Oklahoma’s recent earthquakes and saltwater disposal. *Sci.*  
450 *Adv.* **1**, e1500195 (2015).
- 451 50. Steinberger, B., Schmeling, H. & Marquart, G. Large-scale lithospheric stress field and  
452 topography induced by global mantle circulation. *Earth and Planetary Science Letters* **186**, 75–  
453 91 (2001).

- 454 51. Bahadori, A. & Holt, W. E. Geodynamic evolution of southwestern North America since  
455 the Late Eocene. *Nat Commun* **10**, 5213 (2019).
- 456 52. Becker, T. W. *et al.* Western US intermountain seismicity caused by changes in upper  
457 mantle flow. *Nature* **524**, 458–461 (2015).
- 458 53. Bensen, G. D. *et al.* Processing seismic ambient noise data to obtain reliable broad-band  
459 surface wave dispersion measurements. *Geophysical Journal International* **169**, 1239–1260  
460 (2007).
- 461 54. Agnew, D. C. *SPOTL: Some Programs for Ocean-Tide Loading*. (UC San Diego: Library  
462 – Scripps Digital Collection, 2012).
- 463 55. Ventosa, S., Schimmel, M. & Stutzmann, E. Towards the Processing of Large Data  
464 Volumes with Phase Cross-Correlation. *Seismological Research Letters* (2019)  
465 doi:10.1785/0220190022.
- 466 56. Mao, S., Mordret, A., Campillo, M., Fang, H. & van der Hilst, R. D. On the measurement  
467 of seismic travel-time changes in the time-frequency domain with wavelet cross-spectrum  
468 analysis. *Geophysical Journal International* (2019) doi:10.1093/gji/ggz495.
- 469

# Figures

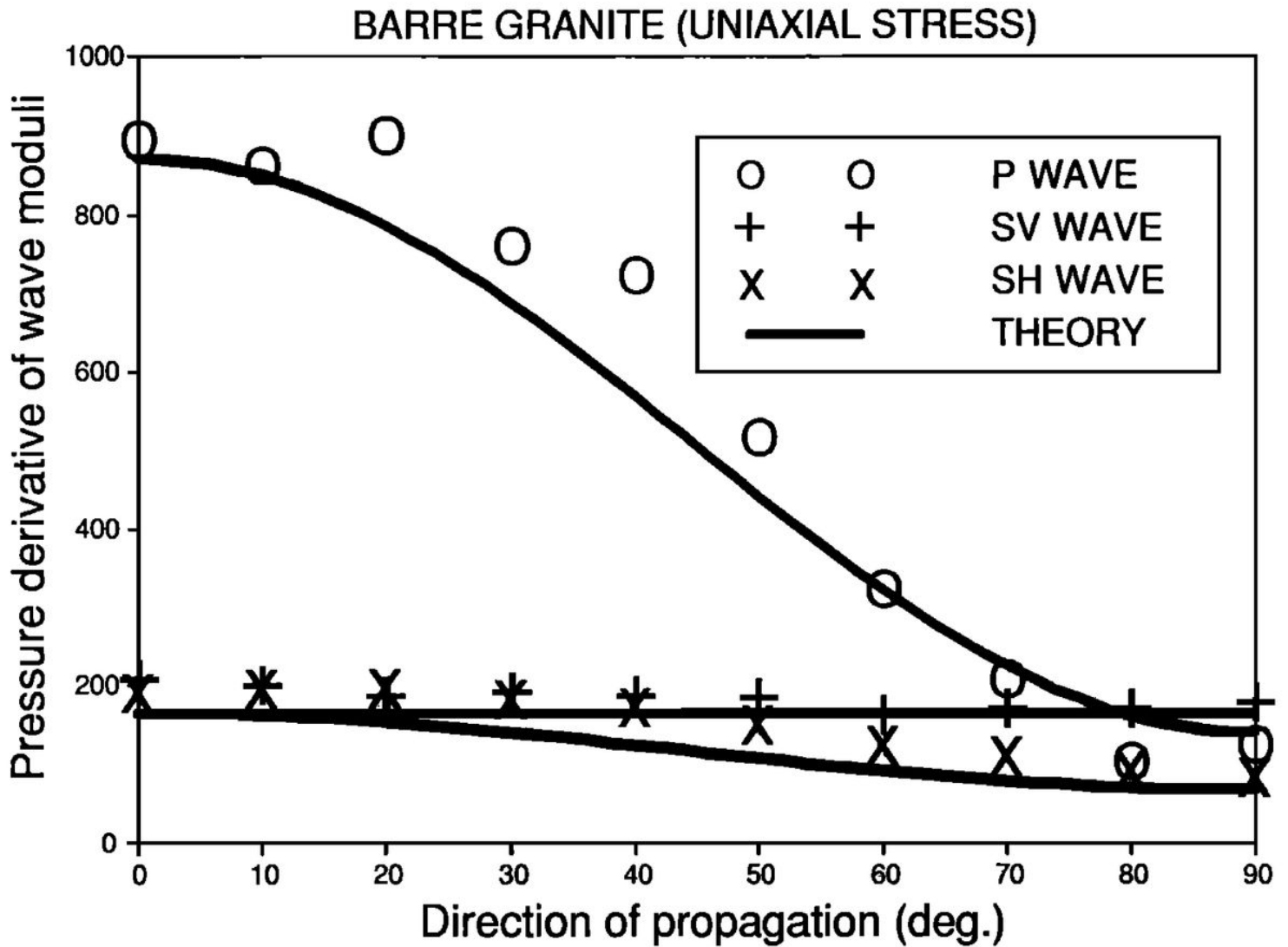
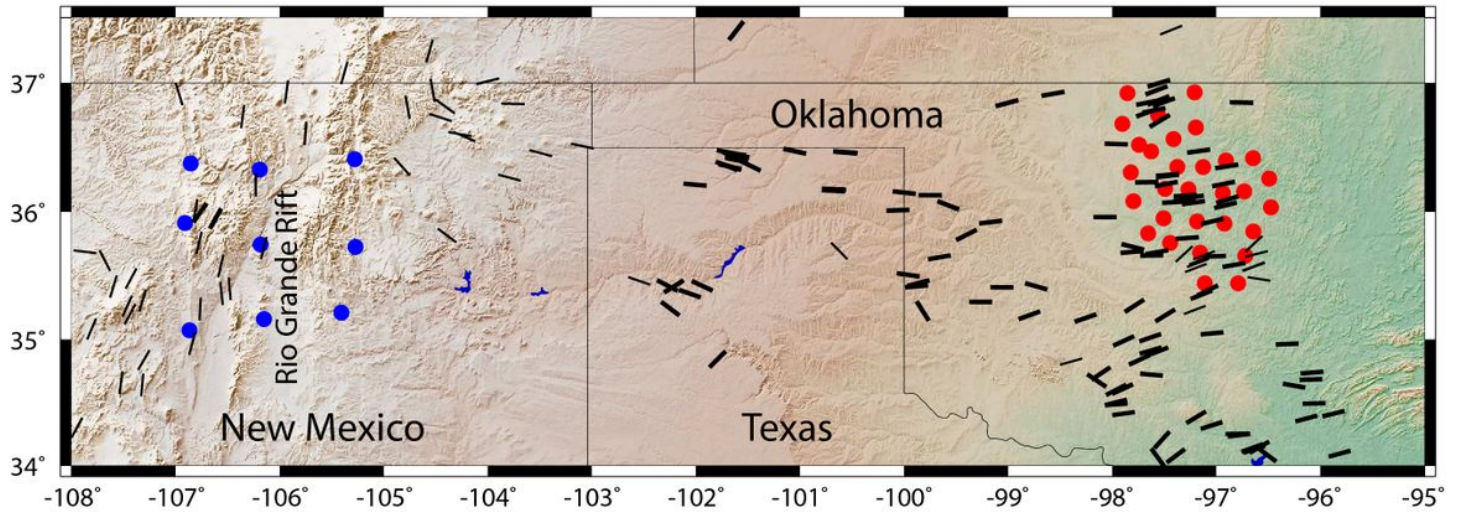
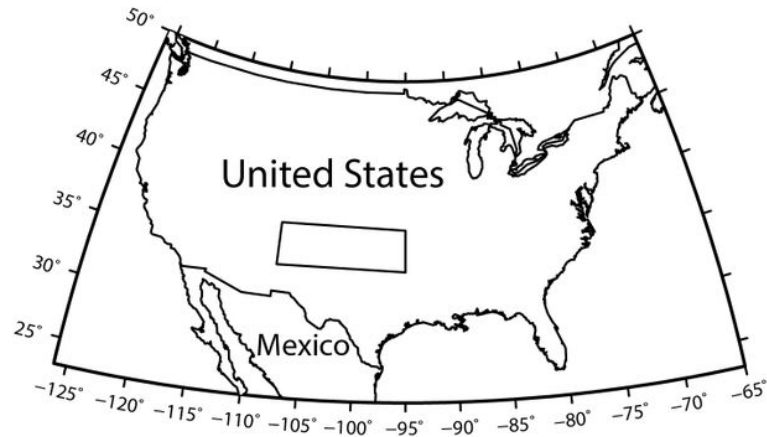


Figure 1

Stress induced anisotropy in Nonlinear Susceptibility from Johnson and Rasolofosaon. The vertical axis represents nonlinear susceptibility. The horizontal axis shows the angle between the orientation of the uniaxial stress and the direction of propagation of the probe wave. (AGU grants permission for individuals to use figures, tables, and short quotes from AGU journal and books for republication in academic works provided full attribution is included.)



**Figure 2**

We measured the azimuthal dependence of nonlinear elastic behavior in north-central New Mexico and north-central Oklahoma. The blue circles are seismic stations from Earthscope’s Transportable Array. The red circles are seismic stations from the Nanometrics Research Array. The short black lines indicate the direction of SHmax for stress indicators used in the 2016 World Stress Map, classes A, B, and C. The thick stress indicator lines are from borehole measurements and the thin stress indicator lines are from earthquake or geologic feature orientations. The rectangle in the top map indicates the position of the bottom map within North America.

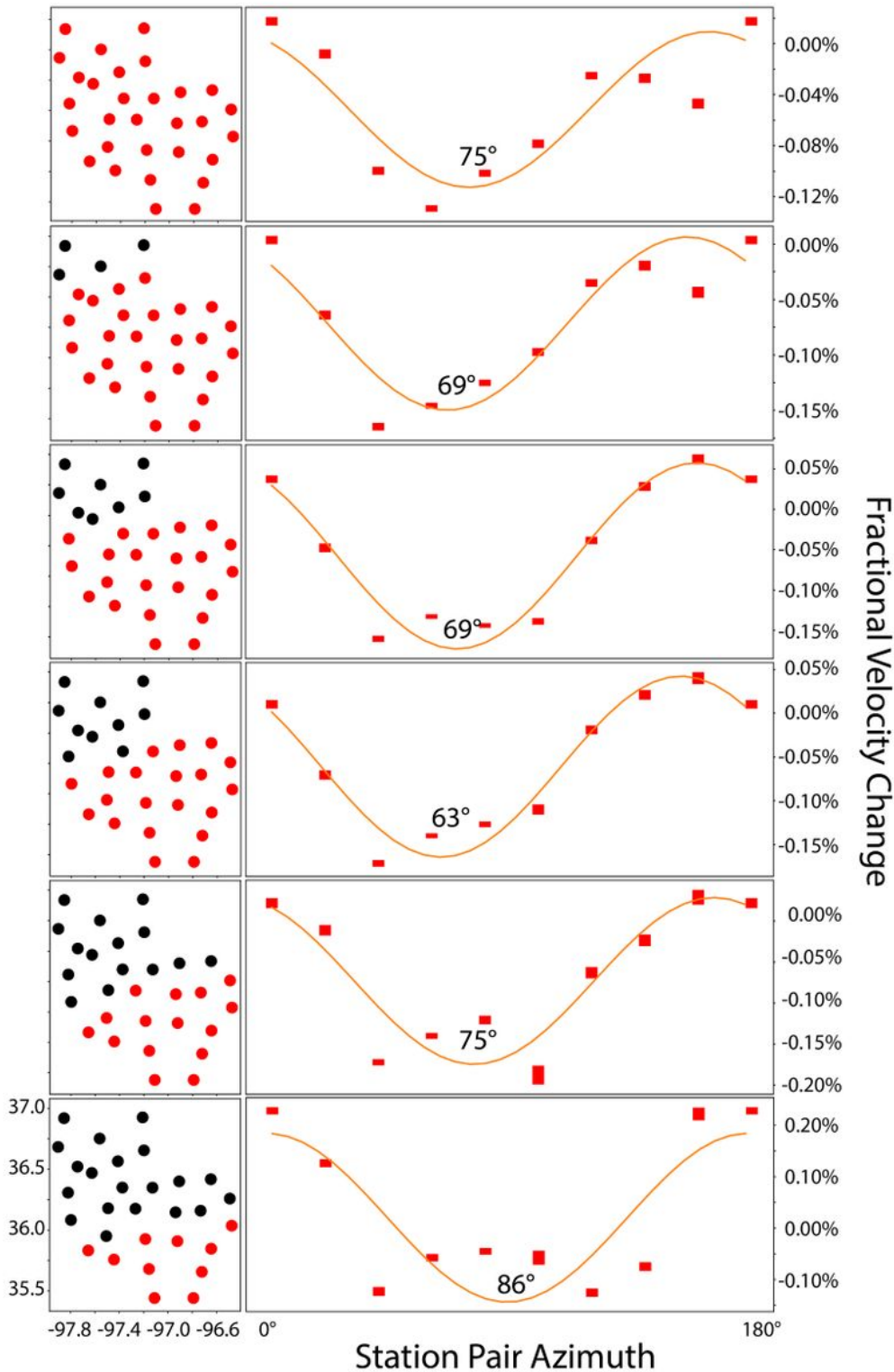


**Figure 3**

Shown are the seismic stations and azimuthal dependence of nonlinear susceptibility in Oklahoma. Red stations in the left panels are used to calculate fractional velocity changes shown on the right (see Fig. 2 for station locations). Vertical red bars represent uncertainties at the 99.5% confidence interval. The orange curve is the best fit sinusoidal function. The value listed is the azimuthal angle of maximum nonlinearity according to the fit sinusoid (negative fractional velocity changes).

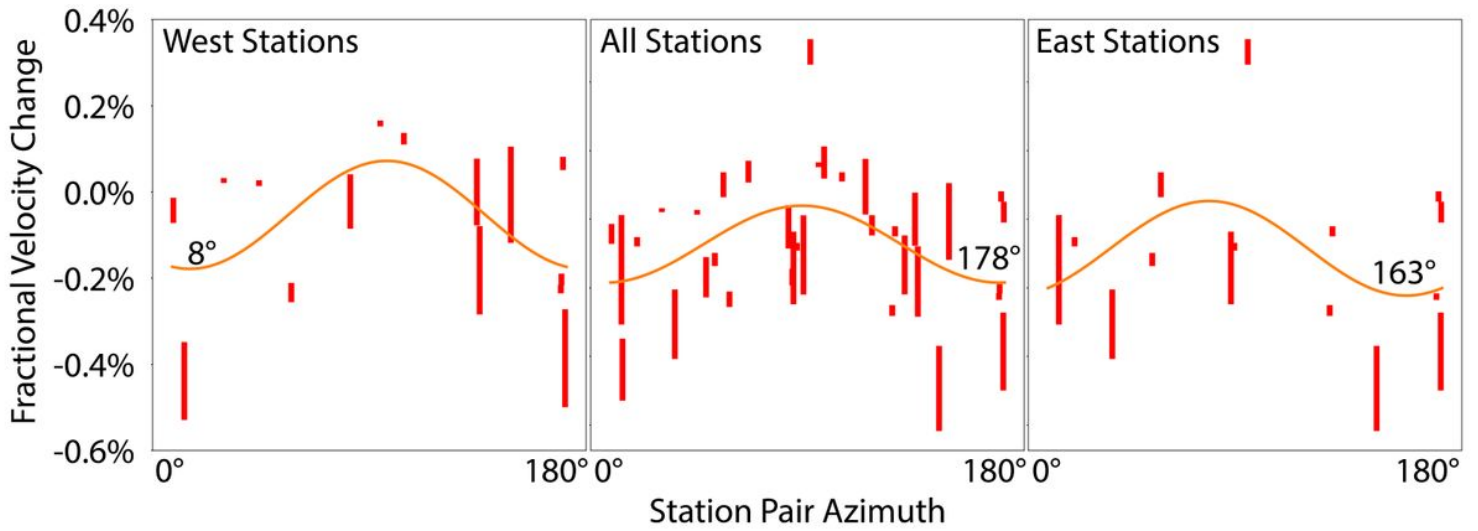
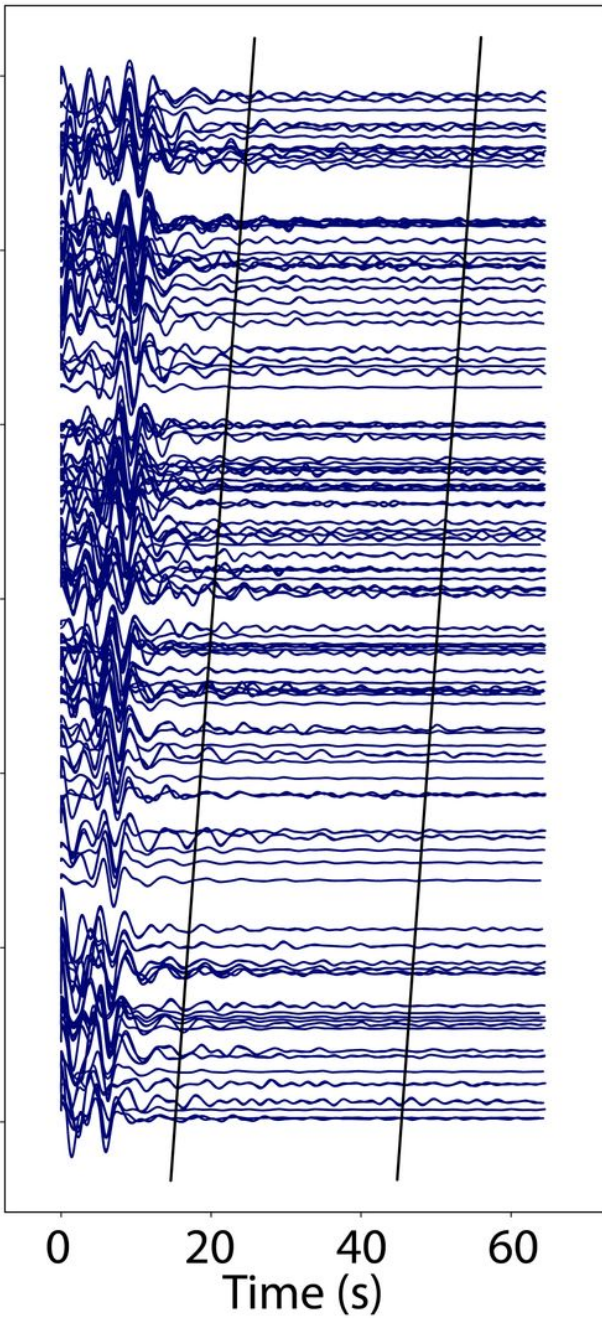


**Figure 4**

Shown is the azimuthal dependence of nonlinear susceptibility in New Mexico. The left, center, and right axes show the results using the 6 western stations, all stations, and the 6 eastern stations, respectively. The orange curve is the best fit sinusoidal function. The vertical red bars represent the fractional velocity change with uncertainties at the 99.5% confidence level for each station pair. The angle value reported on each axis indicates the azimuth with the maximum NS (negative fractional velocity change).

### Oklahoma Waveforms



### New Mexico Waveforms

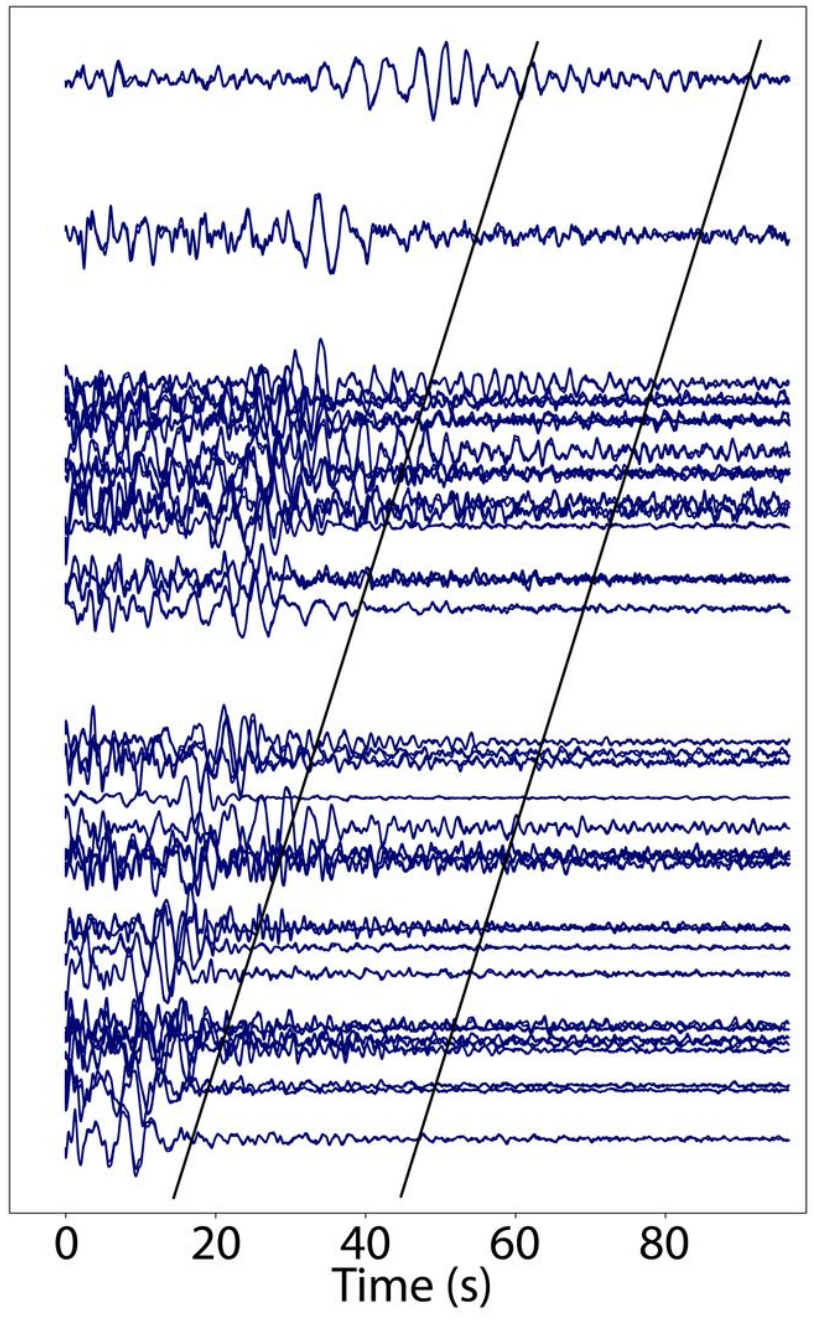


**Figure 5**

Empirical Green's Functions, for Oklahoma (left), and New Mexico (right), ordered by interstation distance. The black lines bracket the coda used for the velocity calculations.